CHINESE OPTICS LETTERS

Vol. 22, No. 5 | May 2024

Double-cliff-layer uni-traveling-carrier photodiode with high responsivity and ultra-broad bandwidth

Yaru Han (韩亚茹)[1,†], Yuxin Tian (田雨欣)[1,†], Bing Xiong (熊 兵)[1,*], Changzheng Sun (孙长征)[1], Jian Wang (王 健)[1], Zhibiao Hao (郝智彪)[1], Yanjun Han (韩彦军)[1,2], Lai Wang (汪 莱)[1], Hongtao Li (李洪涛)[1], Lin Gan (甘 霖)[1], and Yi Luo (罗 毅)[1,2]

[1] Beijing National Research Center for Information Science and Technology (BNRist), Department of Electronic Engineering, Tsinghua University, Beijing 100084, China

[2] Flexible Intelligent Optoelectronic Device and Technology Center, Institute of Flexible Electronics Technology of THU, Jiaxing 314006, China

[†]These authors contributed equally to this work.

*Corresponding author: bxiong@tsinghua.edu.cn

Received October 27, 2023 | Accepted January 3, 2024 | Posted Online May 17, 2024

A novel backside-illuminated double-cliff-layer uni-traveling-carrier (DCL-UTC) photodiode with both high responsivity and ultra-broad bandwidth is designed and demonstrated. A thick absorption layer is adopted for high responsivity, and a depletion region with double cliff layers is proposed to alleviate the space charge effect and maintain overshoot electron velocity under large photocurrents. In addition, inductive coplanar waveguide electrodes are employed to enhance the frequency response performance. The 6-μm-diameter photodiode exhibits a high responsivity of 0.51 A/W and a large 3-dB bandwidth of 102 GHz. A high RF output power of 2.7 dBm is recorded at 100 GHz.

Keywords: uni-traveling-carrier photodiode; high responsivity; broad bandwidth.
DOI: 10.3788/COL202422.052501

1. Introduction

Broad bandwidth photodiodes (PDs) with high-responsivity and high RF output power are key components for microwave/millimeter-wave photonic transmission and processing systems[1,2], in which both wide bandwidth and high link gain with large spurious free dynamic range (SFDR) are necessary. Recently, the increasing demand of millimeter-wave and sub-THz applications has driven the need for PDs with bandwidths over 100 GHz[3–6]. Compared with traditional PIN photodiodes, uni-traveling carrier PDs (UTC-PDs) have demonstrated ultra-broad bandwidth performance due to the elimination of slow hole transportation[7–9]. Waveguide integrated UTC-PDs have been reported to realize ultra-broad bandwidth and high responsivity[10–12], but the saturation power performance is limited. Inserting a thin n-doped layer into the depletion region can compensate the space charge screening effect, resulting in improved saturation characteristics together with a bandwidth over 110 GHz[13–15]. However, as the PD employs a thin absorption region to ensure broad bandwidth performance, its responsivity is relatively low (< 0.2 A/W), which is not suitable to attain high link gain and large SFDR.

In this work, a high-responsivity and ultra-broadband backside-illuminated double-cliff-layer (DCL) uni-traveling-carrier photodiode (UTC-PD) is designed and fabricated. An 850-nm-thick InGaAs absorption layer is adopted for high responsivity. The self-induced electric field in the graded p-doped absorption layer under high photocurrents facilitates electron drift out. Meanwhile, the depletion region with the double-cliff layer is incorporated to tune the electric field distribution, thus mitigating the high-density electron-induced space charge screening effect and maintaining the overshoot electron velocity. An inductive coplanar waveguide (CPW) with optimized length is employed to enhance the frequency response of the device. The fabricated 6-μm-diameter DCL-UTC-PD exhibits a high responsivity of 0.51 A/W and a large 3-dB bandwidth of 102 GHz at a photocurrent of 10 mA. The saturation photocurrent at 100 GHz is measured to be 16 mA, corresponding to an RF power of 2.7 dBm.

2. Epitaxial Structure and CPW Design

The epitaxial structure of the proposed MUTC-PD is shown in Fig. 1(a), which is grown by metal organic chemical vapor deposition (MOCVD) on a semi-insulating InP substrate. To ensure a high-responsivity, the PD adopts a thick absorption region consisting of a 650-nm-thick graded p-doped InGaAs absorption layer and a 200-nm-thick n-doped InGaAs absorptive depletion layer. The responsivity (R) of the detector can be expressed as $R = \frac{q}{h\nu} \times (1 - e^{-\alpha L})$, where $\alpha \approx 0.7\ \mu m^{-1}$ is the absorption coefficient of InGaAs material around 1550 nm, L

is the effective thickness of the absorption layer, q is the electron charge, and $h\nu$ is photon energy. Assuming a back-incidence structure with the top metal acting as a mirror, the absorption thickness is $L = 1.7$ μm since the incident light passes through the absorption region twice. As a result, the 850-nm-thick absorption region leads to a response of 0.87 A/W.

A thick absorption region helps increase the responsivity of the PD, but it tends to lengthen the transit time of photocarriers, thus degrading the bandwidth performance. To realize high-speed performance, the transit time in both the p-doped absorption region and the depletion region should be minimized. A self-induced electric field will be formed in the 650-nm-thick graded p-doped InGaAs absorption layer due to the variation of the Fermi level. Under high photocurrents, the hole drift current would enhance the self-induced electric field, thus leading to drift dominated electron transport and reduced transit time[16,17]. Figure 1(b) shows the calculated electric field within the absorption region. It is evident that the self-induced electric field increases with the photocurrent and can reach up to several kV/cm, thus speeding up electron transport through the absorption region.

To alleviate the space charge screening effect, a double-cliff-layer depletion region is proposed. As shown in Fig. 1(c), the electric field in the depletion region can be effectively elevated by the two n-doped cliff layers, thus improving the saturation performance of the PD, and it would only slightly increase the capacitance of the PD. The electric field profile in the depletion region can be adjusted by judiciously positioning the two cliff layers. The variation of the electric field within the depletion region under different bias voltages is illustrated in Fig. 1(d), where the cliff layers are positioned 100 nm and 200 nm away from the InGaAs and InP interface. A flattened electric field within the depletion region helps improve the saturation performance of the PD. Meanwhile, an electric field in the range 5–30 kV/cm is helpful for maintaining overshoot velocity[18].

The normalized frequency response of a PD can be expressed as $H(\omega) = H_\tau(\omega) \cdot H_{\mathrm{RC}}(\omega)$, where $H_\tau(\omega)$ represents the transit time limited frequency response, while $H_{\mathrm{RC}}(\omega)$ is the RC constant limited frequency response. An inductance can provide improved impedance matching for the capacitive PD, thus enhancing the frequency response. However, implementing inductance at high frequencies is challenging[19]. High-impedance CPW has been proposed as an alternative way to enhance the bandwidth performance of PDs[20,21], which takes advantage of the inductive characteristics of the high-impedance CPW.

In our device, a short section of a 115-Ω-impedance CPW electrode is included to optimize the frequency response of the PD. The schematic and equivalent circuits of the PD with high-impedance CPW structure are shown in Figs. 2(a) and 2(b). The signal electrode width is 6 μm, while the gap between the signal and the ground electrodes is 97 μm. The transit time limited transfer function is simplified to be $H_\tau(\omega) = \frac{1}{1+j\frac{\omega}{2\pi f_{\mathrm{tr}}}}$, where $f_{\mathrm{tr}} = 87$ GHz. The RC constant is referred from our previous 6-μm-diameter PDs with 106 GHz bandwidth, as the thickness of the depletion layer and PD area are similar here[22]. The junction capacitance is $C_j = 4$ fF, the parasitic capacitance is $C_p = 16$ fF, the junction resistance is set to $R_j = 20$ kΩ, and the electrode contact resistance is $R_1 = 5$ Ω. The RC constant limited

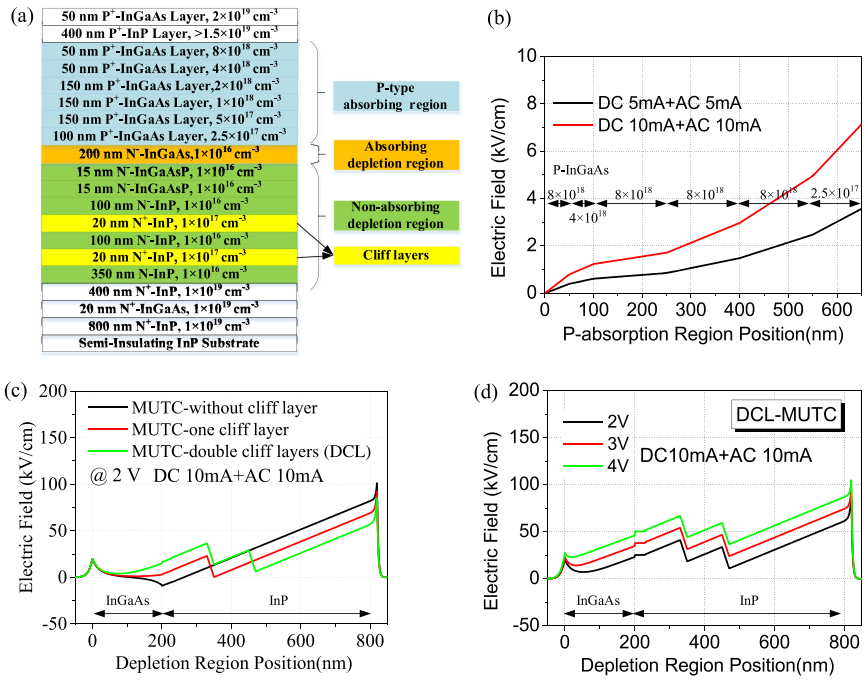

Fig. 1. (a) Epitaxial layer structure of the DCL-UTC-PD. (b) Photocurrent induced electric field distribution in the 650-nm-thick p-doped absorption region. Electric field in the depletion region of (c) traditional UTC-PD and (d) DCL-UTC-PD structure under a photocurrent of 10 mA and different bias voltages.

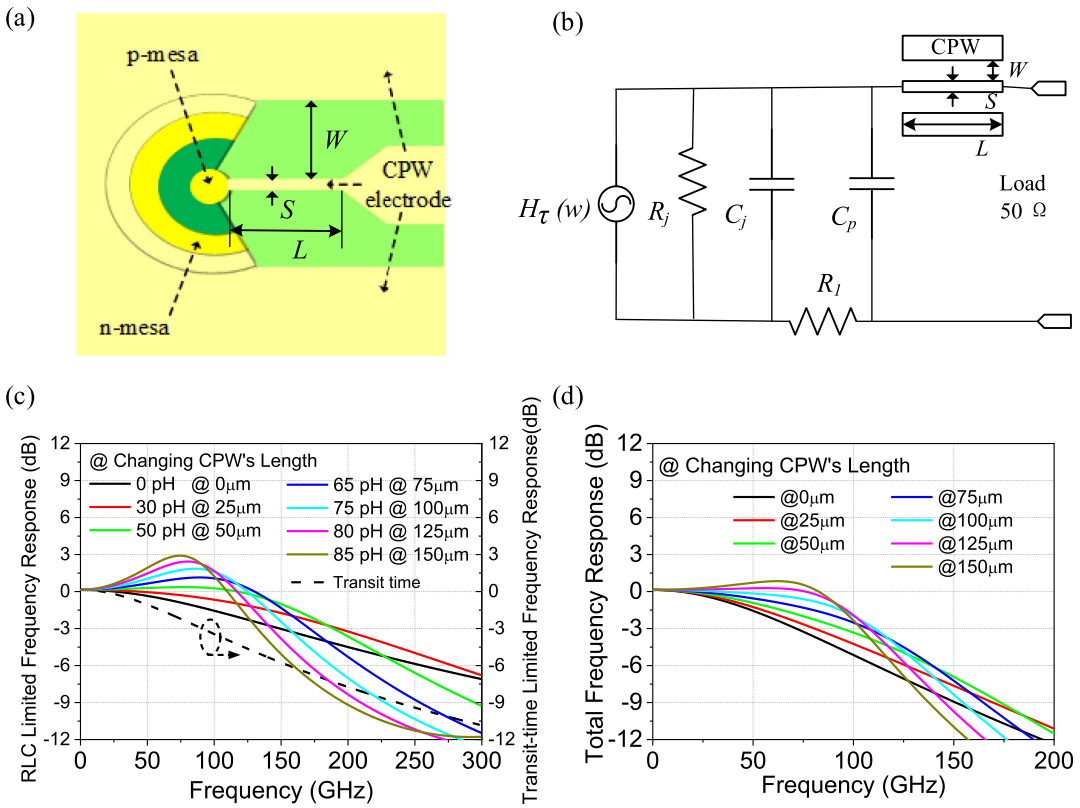

Fig. 2. (a) Schematic and (b) equivalent circuit of the PD with high-impedance CPW structure. (c) RLC and transit time limited frequency responses of the PD with different CPW lengths. (d) Total frequency responses of the PD with different CPW lengths.

bandwidth of the PD without the CPW is estimated to be 150 GHz. The introduction of inductive CPW helps achieve better impedance matching by compensating the capacitance of the PD, thus enhancing the frequency response, especially at low frequencies. Figures 2(c) and 2(d) show the RLC limited frequency responses and the total frequency responses of the PD with different lengths of CPW. As the length of the high-impedance CPW increases from 0 to 75 μm, the RC constant limited bandwidth increases from 150 GHz to 170 GHz, and the total bandwidth is enhanced to 107 GHz. Increasing the CPW length to 100 μm results in a slightly decreased RC constant limited bandwidth. Nevertheless, the entire device exhibits an improved bandwidth, as the transfer function $H_{RC}(\omega)$ below the LC resonance peak is enhanced at the price of reduced response at higher frequencies. Further increasing the CPW length would reduce the overall bandwidth of the PD. Consequently, a 100-μm-long 115-Ω CPW is adopted as the optimized structure for our device.

3. Device Fabrication and Measurement

Backside-illuminated DCL-MUTC-PDs are fabricated with a 3-mesa structure for structural stability after wet-etching reported in our previous work[23], as illustrated in Fig. 3(a). Both p- and n-mesas are patterned by a combined inductively coupled plasma (ICP) dry-etching and wet-etching process. Ti/Pt/Au and Ni/Au are sputtered as the p- and n-electrodes, respectively. An 800-nm-thick SiO_2 layer is deposited for sidewall passivation and parasitic capacitance reduction. Then high-impedance CPW is formed on the SiO_2 layer by sputtering and electroplating. Finally, the device is thinned and back polished, and a 215-nm-thick SiN_x layer (refractive index ~1.8) is deposited on the backside of the device to reduce incident light reflection down to 1%.

The responsivity of the fabricated device is 0.51 A/W for 6-μm-diameter PDs and 0.56 A/W for 8-μm-diameter ones, respectively. The divergence angle of the optical fiber used in our test is 15°, and the diameter of the optical field is expanded to about 17 μm after propagating through the 100-μm-thick InP substrate. As a result, the measured responsivity is lower than the simulation value of 0.84 A/W. In the future, a substrate lens can be incorporated to improve the responsivity[24].

The frequency response and RF output power are measured with a two-laser heterodyne measurement system[25]. A set of microwave and millimeter-wave sensor heads is used to cover the frequency range from DC to 40 GHz, 50–75 GHz, and 75–110 GHz. The frequency response at −2 V is shown in Fig. 3(b). The 3-dB bandwidth is only 85 GHz at a photocurrent of 5 mA, while a 3-dB bandwidth as large as 102 GHz is recorded at a photocurrent of 10 mA. The output RF power as a function of photocurrent is plotted in Fig. 3(c). The photocurrent at the 1-dB compression point is 16 mA at −3 V bias voltage, corresponding to an RF output power of 2.7 dBm. To the best of

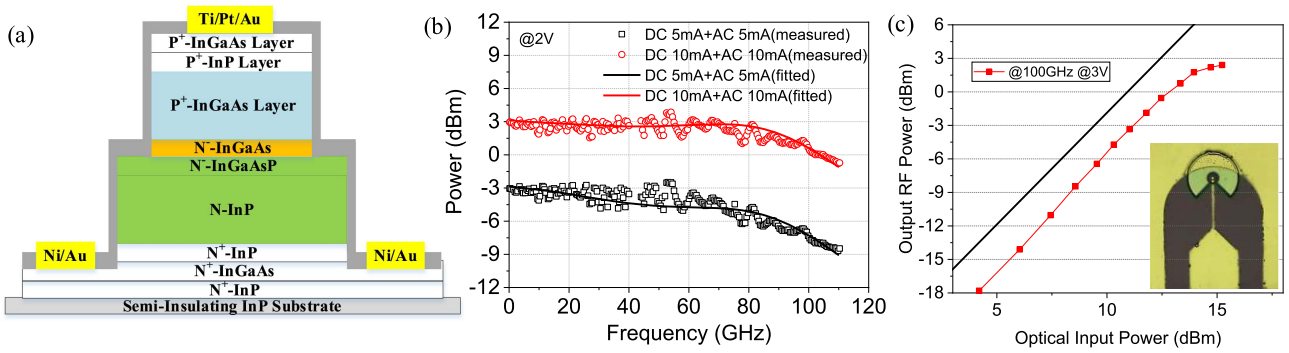

Fig. 3. (a) Schematic view of the PD structure. (b) Frequency responses at different photocurrents under a bias voltage of 2 V. (c) Output RF power versus the optical input power. The inset is the microscope image of the 6-μm-diameter PD.

our knowledge, this is the best performance reported for back-side-illuminated PDs with such high responsivity and wide bandwidth.

4. Equivalent Circuit Model Analysis

Figure 4(a) shows the equivalent circuit model with variable RC parameters[14], which takes both the transit time (Region 1) and RC electric circuit parameters (Region 2) into consideration. First, the parameters of Region 2 are tuned to fit the measured S_{22}, and the transit time of Region 1 can then be extracted by fitting the measured frequency response S_{12}. R_u and C_u are the resistance and capacitance of the 200 nm InGaAs and 30 nm InGaAsP depletion layer, which are extracted as 20 kΩ and 30 fF, respectively. R_j and C_j are the resistance and capacitance of the 590 nm InP depletion layer. During the fitting process, the bulk material resistance R_1 and the contact resistance R_2 are extracted as 3 Ω and 8 Ω, respectively. The capacitance $C_j = 4$ fF, while the parasitic capacitance of the p-electrode $C_p = 17$ fF. Fairly good agreement between the measured and simulated S_{22} curves is shown in Figs. 4(b)–4(d).

The bandwidths under different bias voltages and photocurrents are shown in Fig. 5(a). The variation of bandwidth with the photocurrent is mainly attributed to the space charge screening effect in the depletion region and the self-induced electric field in the p-absorption region. The self-induced electric field under a high photocurrent helps maintain a high electron drift velocity in the p-doped absorption region, while the double cliff layers

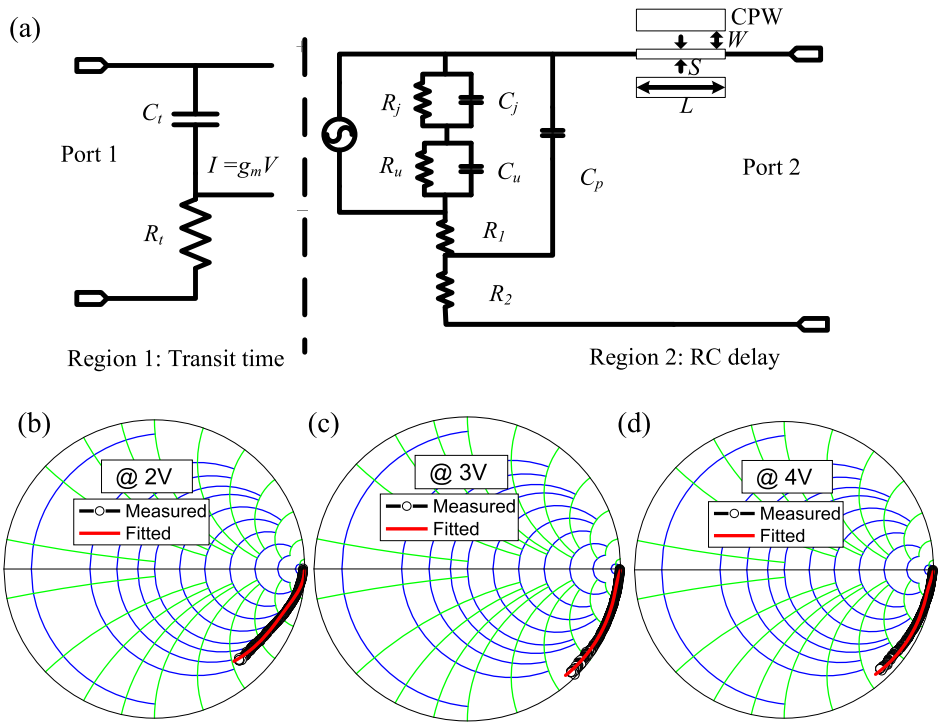

Fig. 4. (a) Equivalent circuit of the PD with CPW structure. (b)–(d) Measured and fitted S_{22} parameters (0–40 GHz) of the PD under different reverse biases.

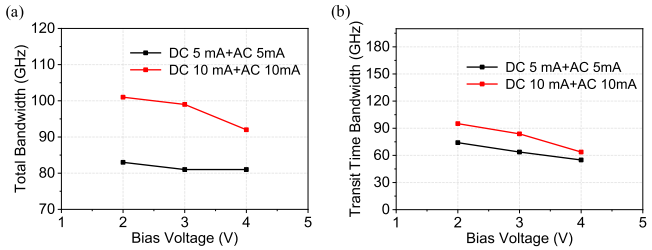

Fig. 5. (a) Total bandwidth and (b) transit time limited bandwidth under different bias voltages and photocurrents.

inserted into the depletion region can alleviate the space charge screening effect and ensure a suitable electric field for an overshoot drift velocity under high photocurrents. The RC limited bandwidth of Region 2 is estimated to be 145 GHz.

The extracted transit time limited bandwidth $f_{tr} = 1/(2\pi R_t C_t)$ is shown in Fig. 5(b). The transit time limited bandwidth under 10 mA photocurrent is larger than that under 5 mA, which is attributed to the enhanced self-induced electric field. Under −2 V bias voltage and 5 mA photocurrent, the transit time limited bandwidth is 74 GHz, corresponding to a transit time of 6.0 ps. When the photocurrent is increased to 10 mA, the transit time limited bandwidth increases to 95 GHz, corresponding to a transit time of 4.7 ps. Assuming an overshoot drift velocity of 3×10^5 m/s for electrons in the depletion region, the electron velocities in the p-doped region under 5 and 10 mA photocurrent are extracted to be 2×10^5 and 3.3×10^5 m/s, respectively.

According to the above analysis, the large photocurrent helps to maintain a high drift velocity of electrons in the p-type absorption region, while the insertion of the double cliff layers into the depletion region can alleviate the space-charge screening effect and ensure electron velocity overshoot under large photocurrents. Figure 6 summarizes the responsivity versus frequency of back-illuminated PDs reported in the literature.

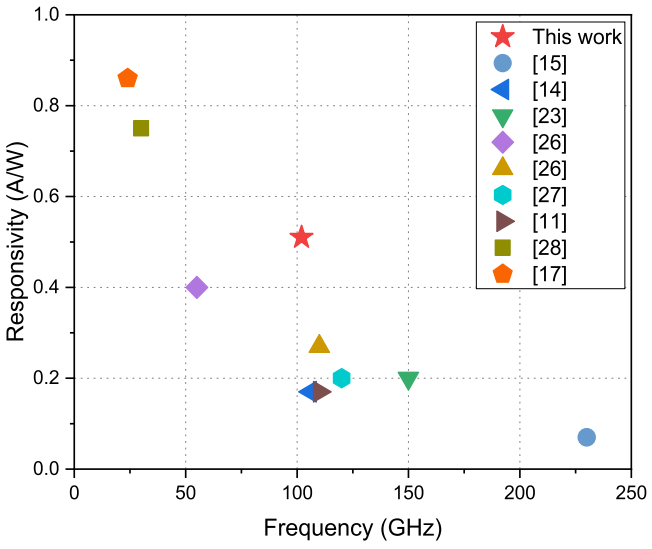

Fig. 6. Responsivity versus frequency of back-illuminated PDs.

The proposed DCL-UTC photodiode shows the highest responsivity with ~100 GHz bandwidth[11,14,15,17,23,26–28].

5. Summary

In conclusion, a broad bandwidth DCL-UTC-PD with high-responsivity and high saturation power is proposed and demonstrated. High responsivity is achieved by adopting an 850-nm-thick InGaAs absorption structure. The graded p-doped absorption layer is designed to ensure an enhanced self-induced electric field under high photocurrent conditions, thus facilitating electron drift out of the region. Meanwhile, double cliff layers are inserted into the depletion region to compensate the high electron density induced space charge screening effect and maintain overshoot electron velocity. In addition, a high-impedance CPW with optimized length is employed to enhance the frequency response of the PD. The fabricated 6-μm-diameter DCL-UTC-PD exhibits a high responsivity of 0.51 A/W and a maximum 3-dB bandwidth of 102 GHz with a standard 50 Ω load. The saturation photocurrent at 100 GHz is 16 mA, corresponding to an RF output power of 2.7 dBm.

Acknowledgements

This work was supported in part by the National Key R&D Program of China (No. 2022YFB2803002), National Natural Science Foundation of China (Nos. 62235005, 62127814, 62225405, 61975093, 61927811, 61991443, and 61974080), and Collaborative Innovation Center of Solid-State Lighting and Energy-Saving Electronics.

References

1. J. Yao, "Microwave photonics," J. Lightwave Technol. **27**, 314 (2009).
2. A. Stöhr, S. Babiel, P. J. Cannard, *et al.*, "Millimeter-wave photonic components for broadband wireless systems," IEEE Trans. Microw. Theory Tech. **58**, 3071 (2010).
3. J.-W. Shi, C.-B. Huang, and C.-L. Pan, "Millimeter-wave photonic wireless links for very high data rate communication," NPG Asia Mater. **3**, 41 (2011).
4. S. Koenig, D. Lopez-Diaz, J. Antes, *et al.*, "Wireless sub-THz communication system with high data rate," Nat. Photonics **7**, 977 (2013).
5. A. J. Seeds, H. Shams, M. J. Fice, *et al.*, "Terahertz photonics for wireless communications," J. Lightwave Technol. **33**, 579 (2014).
6. T. Umezawa, A. Kanno, K. Kashima, *et al.*, "Bias-free operational UTC-PD above 110 GHz and its application to high baud rate fixed-fiber communication and W-band photonic wireless communication," J. Lightwave Technol. **34**, 3138 (2016).
7. T. Nagatsuma, H. Ito, and T. Ishibashi, "High-power RF photodiodes and their applications," Laser Photonics Rev. **3**, 123 (2009).
8. T. Ishibashi and H. Ito, "Uni-traveling-carrier photodiodes," J. Appl. Phys. **127**, 031101 (2020).
9. T. Shi, B. Xiong, C. Sun, *et al.*, "Study on the saturation characteristics of high-speed uni-traveling-carrier photodiodes based on field screening analysis," Chin. Opt. Lett. **9**, 082302 (2011).
10. E. Rouvalis, C. C. Renaud, D. G. Moodie, *et al.*, "Continuous wave terahertz generation from ultra-fast InP-based photodiodes," IEEE Trans. Microw. Theory Tech. **60**, 509 (2012).
11. Q. Li, K. Li, Y. Fu, *et al.*, "High-power flip-chip bonded photodiode with 110 GHz bandwidth," J. Lightwave Technol. **34**, 2139 (2016).

12. C. Renaud, D. Moodie, M. Robertson, *et al.*, "High output power at 110 GHz with a waveguide uni-travelling carrier photodiode," in *LEOS 2007–IEEE Lasers and Electro-Optics Society Annual Meeting Conference Proceedings* (2007), p. 782.
13. Q. Li, K. Li, Y. Fu, *et al.*, "High-power flip-chip bonded photodiode with 110 GHz bandwidth," J. Lightwave Technol. **34**, 2139 (2016).
14. J. Li, B. Xiong, Y. Luo, *et al.*, "Ultrafast dual-drifting layer uni-traveling carrier photodiode with high saturation current," Opt. Express **24**, 8420 (2016).
15. Y. Tian, B. Xiong, C. Sun, *et al.*, "Ultrafast MUTC photodiodes over 200 GHz with high saturation power," Opt. Express **31**, 23790 (2023).
16. W. Xin, D. Ning, C. Hao, *et al.*, "InGaAs–InP photodiodes with high responsivity and high saturation power," IEEE Photon. Technol. Lett. **19**, 501 (2007).
17. T. Shi, B. Xiong, C. Sun, *et al.*, "Back-to-back UTC-PDs with high responsivity, high saturation current and wide bandwidth," IEEE Photon. Technol. Lett. **25**, 136 (2012).
18. T. J. Maloney and J. Frey, "Transient and steady-state electron transport properties of GaAs and InP," J. Appl. Phys. **48**, 781 (1977).
19. U. Westergren, R. Schatz, and E. Berglind, "Design of inductive pin diode matching for optical receivers with increased bit-rate operation," J. Lightwave Technol. **19**, 1956 (2001).
20. Q. Zhou, A. S. Cross, A. Beling, *et al.*, "High-power V-band InGaAs/InP photodiodes," IEEE Photon. Technol. Lett. **25**, 907 (2013).
21. M. Anagnosti, C. Caillaud, F. Blache, *et al.*, "Optimized high speed UTC photodiode for 100 Gbit/s applications," IEEE J. Sel. Top. Quantum Electron. **20**, 29 (2014).
22. J. Li, B. Xiong, C. Sun, *et al.*, "Analysis of frequency response of high power MUTC photodiodes based on photocurrent-dependent equivalent circuit model," Opt. Express **23**, 21615 (2015).
23. E. Chao, B. Xiong, C. Sun, *et al.*, "D-band MUTC photodiodes with flat frequency response," IEEE J. Sel. Top. Quantum Electron. **28**, 3802208 (2021).
24. J.-W. Shi, F. M. Kuo, C. J. Wu, *et al.*, "Extremely high saturation current-bandwidth product performance of a near-ballistic uni-traveling-carrier photodiode with a flip-chip bonding structure," IEEE J. Quantum Electron. **46**, 80 (2010).
25. S. Demiguel, L. Giraudet, L. Joulaud, *et al.*, "Evanescently coupled photodiodes integrating a double-stage taper for 40-Gb/s applications-compared performance with side-illuminated photodiodes," J. Lightwave Technol. **20**, 2004 (2002).
26. M. Anagnosti, C. Caillaud, F. Blache, *et al.*, "Optimized high speed UTC photodiode for 100 Gbit/s applications," IEEE J. Sel. Top. Quantum Electron. **20**, 29 (2014).
27. J. S. Morgan, K. Sun, Q. Li, *et al.*, "High-power flip-chip bonded modified uni-traveling carrier photodiodes with −2.6 dBm RF output power at 160 GHz," in *IEEE Photonics Conference (IPC)* (2018), p. 1.
28. X. Wang, N. Duan, H. Chen, *et al.*, "InGaAs–InP photodiodes with high responsivity and high saturation power," IEEE Photon. Technol. Lett. **19**, 1272 (2007).